Low-temperature structural investigations of the frustrated quantum antiferromagnets $Cs_2Cu(Cl_{4-x}Br_x)$

N. van Well,[1] K. Foyevtsova,[2,3] S. Gottlieb-Schönmeyer,[4] F. Ritter,[1] R. S. Manna,[1,*] B. Wolf,[1] M. Meven,[5,6] C. Pfleiderer,[4] M. Lang,[1] W. Assmus,[1] R. Valentí,[3] and C. Krellner[1,†]

[1]*Physikalisches Institut, Goethe-Universität Frankfurt, D-60438 Frankfurt am Main, Germany*

[2]*Quantum Matter Institute, University of British Columbia, Vancouver, British Columbia V6T 1Z4, Canada*

[3]*Institut für Theoretische Physik, Goethe-Universität Frankfurt, D-60438 Frankfurt am Main, Germany*

[4]*Physik-Department E21, TU München, D-85748 Garching, Germany*

[5]*Institut für Kristallographie, RWTH Aachen, D-52056 Aachen, Germany*

[6]*Jülich Centre for Neutron Science at Heinz Maier-Leibnitz Zentrum, D-85747 Garching, Germany*

Powder x-ray diffraction (PXRD) and single-crystal neutron scattering were used to study in detail the structural properties of the $Cs_2Cu(Cl_{4-x}Br_x)$ series, good realizations of layered triangular antiferromagnets. Detailed temperature-dependent PXRD reveal a pronounced anisotropy of the thermal expansion for the three different crystal directions of the orthorhombic structure without any structural phase transition down to 20 K. Remarkably, the anisotropy of the thermal expansion varies for different x, leading to distinct changes of the geometry of the local Cu environment as a function of temperature and composition. The refinement of the atomic positions confirms that for $x = 1$ and 2, the Br atoms occupy distinct halogen sites in the $[CuX_4]$ tetrahedra ($X = $ Cl, Br). The precise structure data are used to calculate the magnetic exchange couplings using density functional methods for $x = 0$. We observe a pronounced temperature dependence of the calculated magnetic exchange couplings, reflected in the strong sensitivity of the magnetic exchange couplings on structural details. These calculations are in good agreement with the experimentally established values for Cs_2CuCl_4 if one takes the low-temperature structure data as a starting point.

PACS number(s): 61.05.C−, 75.10.Jm, 75.50.Ee

I. INTRODUCTION

Cs_2CuCl_4 and Cs_2CuBr_4 are experimental realizations of two-dimensional triangular-lattice spin-$\frac{1}{2}$ Heisenberg antiferromagnets, which have been intensively studied in recent years due to their unconventional magnetic properties at low temperatures. Despite their structural similarities, Cs_2CuCl_4 shows a pronounced spin-liquid behavior at low magnetic fields as well as a Bose-Einstein condensation of magnons at a critical field [1–4], whereas Cs_2CuBr_4 has localized magnetic excitations with well-defined plateaus in the magnetization [5,6]. This situation indicates that the magnetic properties are highly sensitive to small details of the crystal structure, which, so far, has been established only at room temperature [7,8].

The important magnetic units in these systems are Jahn-Teller distorted (CuX_4) tetrahedra ($X = $ Cl, Br), which are arranged in layers separated by the alkali atoms. A deep understanding of the relationship between crystal structure and electronic and magnetic behavior in the series $Cs_2Cu(Cl_{4-x}Br_x)$ requires a detailed structural analysis as a function of x and temperature. Therefore we started the crystal growth of the mixed system $Cs_2Cu(Cl_{4-x}Br_x)$ with a systematic substitution of Cl by Br for $0 \leqslant x \leqslant 4$. It was shown that the orthorhombic structure type ($Pnma$) characterized by triangular-lattice spin-$\frac{1}{2}$-layers can be obtained from aqueous

solution over the whole range of x if the growth temperature is above $50\,°C$ [9]. The magnetic properties and sterical considerations suggested distinct magnetic regimes through a site-selective substitution of the Br atoms on the three different crystallographic halogen positions [9,10]. However, up to now no direct structural evidence for such a scenario has been given and the detailed crystal structures at low temperature have not been available except the lattice parameters for $x = 0$ [1,2].

The purpose of the present work is to gain detailed information on the structural properties of $Cs_2Cu(Cl_{4-x}Br_x)$ at low temperatures by means of x-ray and neutron diffraction experiments. In particular, we are specially interested in identifying any structural phase transition that might occur upon lowering the temperature as the orthorhombic structure was found to be metastable for $0 \leqslant x < 4$ [9]. Furthermore, we determine accurately the crystal structure parameters for $x = 0, 1, 2,$ and 4. In addition, we perform density functional theory (DFT) calculations using the identified crystal structures and investigate the various superexchange couplings between Cu spins. In previous DFT calculations, it was demonstrated that the superexchange couplings sensitively depend on fine structural details of the local Cu environment given by the $[CuX_4]$ tetrahedra (X denotes the halogen atom, Cl or Br) [11]. This indicates that even in the absence of a structural phase transition, magnetic interactions in $Cs_2Cu(Cl_{4-x}Br_x)$ might be strongly modified by temperature-induced structural variations. One of the main findings of the present study is that the latter effect is indeed strong in Cs_2CuCl_4, and the DFT calculations with the correct low-temperature crystal structure can reproduce the experimental coupling constants.

———————
*Present address: EP VI, Center for Electronic Correlations and Magnetism, Augsburg University, Germany.

†krellner@physik.uni-frankfurt.de

The paper is organized in the following way. In Sec. II, we provide experimental details of the crystal growth and the structural characterization. The low-temperature PXRD data of the $Cs_2Cu(Cl_{4-x}Br_x)$ mixed system are presented in Sec. III, followed by a detailed structural analysis of the local Cu environment in Sec. IV. Finally, we discuss the temperature dependence of the spin superexchange coupling constants of Cs_2CuCl_4 in Sec. V by performing DFT calculations using the 300 and 20 K crystallographic data, followed by our conclusions.

II. EXPERIMENTAL DETAILS

The $Cs_2Cu(Cl_{4-x}Br_x)$ crystals with an orthorhombic structure were grown from aqueous solution at $50\,°C$ with the evaporation method [9]. Typical crystals for $x = 1$ and 2 are shown in Fig. 1, their growth time lasts around two months.

For the low-temperature powder x-ray diffraction (PXRD), a Siemens D500 diffractometer with CuK_α radiation was used. Cooling of the powder was realized with a closed-cycle helium refrigerator. The measurements were started at 280 K followed by subsequent cooling in 20 K steps down to 20 K (see Fig. 2). At each temperature, T, the sample holder with the powder was thermalized, prior to the measurement scan, employing an in-situ temperature controller. Each powder sample was obtained by milling one single crystal and mixing it with powder of silicon. The latter was used as an internal standard for the temperature dependent correction of the zero shift and the displacement of the powder. Structural parameters were refined from the PXRD data using the GSAS Suite of Rietveld programs [12]. A detailed view of the raw data for $x = 2$ together with the refinement curves are presented in the Appendix. The determination of the low-temperature structure was done for four different concentrations with nominal values of $x = 0,1,2,4$. Microprobe analysis confirmed that these nominal values are close to the actual ones (see Ref. [9]). The measurements of the uniaxial thermal expansion coefficient $\alpha = l^{-1}(\partial l/\partial T)$, where l denotes the sample length, were conducted by employing a high-resolution capacitive dilatometer with a maximum resolution of $\Delta l/l = 10^{-10}$, built after Ref. [13].

Neutron scattering experiments at 300 K were carried out for one single crystal with $x = 1$ at the four-circle-diffractometer HEIDI at the FRM II. A full sphere up to $2\Theta = 65\,°$ was measured with a neutron wavelength of $\lambda = 0.87$ Å (in total 1014 reflexes). The neutron data was refined using the software JANA2006 [14]. One of the measured peaks together with a summary of the obtained and calculated structure-factor amplitudes are presented in the Appendix.
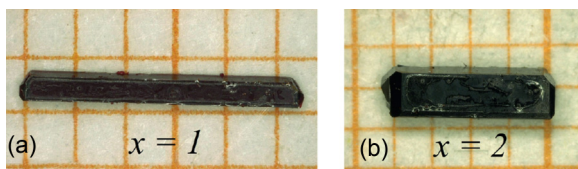

FIG. 1. (Color online) Optical images of the as-grown orthorhombic ($Pnma$) crystals, (a) $Cs_2CuCl_3Br_1$ and (b) $Cs_2CuCl_2Br_2$, obtained from aqueous solution at $50\,°C$. The given scale is 1 mm.
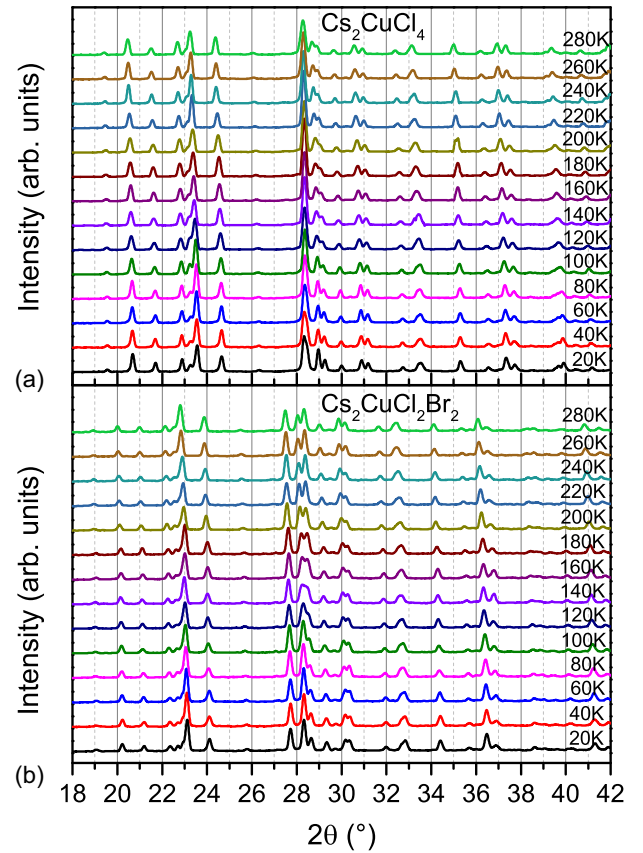

FIG. 2. (Color online) PXRD data from 280 to 20 K exemplarily shown for (a) Cs_2CuCl_4 and (b) $Cs_2CuCl_2Br_2$. No structural phase transition for any of the materials was observed between 280 and 20 K. The high quality of these data allows for the determination of the thermal expansion coefficients.

III. LOW-TEMPERATURE STRUCTURAL CHARACTERIZATION

PXRD was measured and analyzed from 280 to 20 K for selected members of the $Cs_2Cu(Cl_{4-x}Br_x)$ series. Besides the end members ($x = 0$ and 4), the compositions $Cs_2CuCl_3Br_1$ and $Cs_2CuCl_2Br_2$ were chosen for a detailed structural characterization, because for these compounds a partially ordered distribution of the halogen components with respect to the different crystallographic positions was suggested [10]. The complete PXRD data for two of the four different concentrations are shown in Fig. 2. These data clearly indicate that the orthorhombic structure ($Pnma$) of the crystals remains stable down to 20 K without any indication for a structural phase transition between 280 and 20 K. The high quality of these data allows for a detailed analysis of the structural parameters as function of temperature.

From the temperature-dependent PXRD data in Fig. 2, we derived the lattice parameters $l_i = a,b,c$. The variation of these parameters with temperature is shown in Fig. 3 by plotting the $l_i(T)$ data normalized to their values at 280 K, $l_i(T)/l_i(280\,K)$. The T dependence of the lattice parameters was fitted with a third-order polynomial function, because inflection points are apparent. These polynomial functions are later used to determine the coefficients of the thermal expansion and are
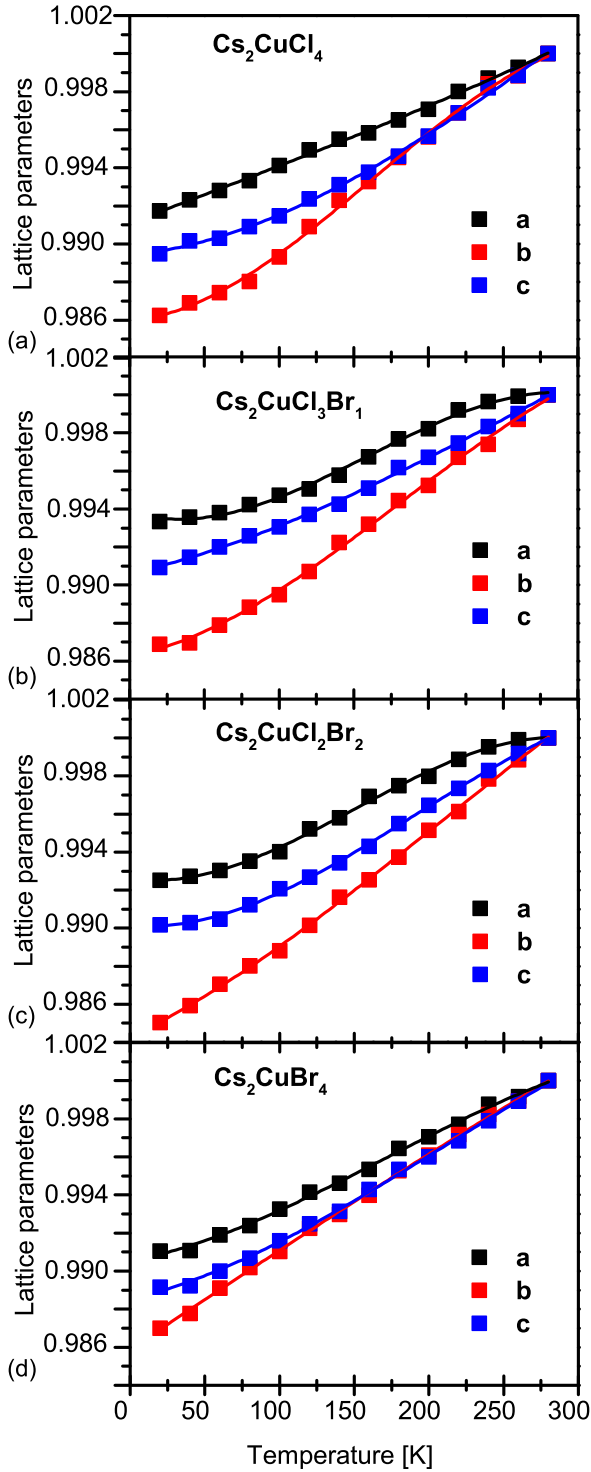
FIG. 3. (Color online) Normalized lattice parameters for (a) Cs_2CuCl_4, (b) $Cs_2CuCl_3Br_1$, (c) $Cs_2CuCl_2Br_2$, and (d) Cs_2CuBr_4, plotted as $l_i(T)/l_i(280\,\text{K})$. The size of each point exceeds the statistical error. The T dependence was fitted with a third-order polynomial function (solid lines), which were used to calculate the coefficients of the thermal expansion.

shown as solid lines in Fig. 3. It is obvious from this figure that $l_i(T)/l(280\,\text{K})$ is anisotropic and changes drastically with increasing x. For $x = 0$, $a(T)$ is linear in temperature down to 20 K, which markedly changes for $x = 1$ and 2. For $b(T)$

this trend is reversed, since for $x = 0$ we observe a strong deviation from a linear-T dependence while as x increases this dependence becomes more linear. The overall anisotropy of the normalized lattice parameters at 20 K is small for $x = 4$, but larger for $x = 2$, due to a larger $a(20\,\text{K})/a(280\,\text{K})$ and a smaller $b(20\,\text{K})/b(280\,\text{K})$ value. This is a further indication for a selective occupation of the halogen positions by Cl and Br as will be discussed in more detail in Sec. IV. Another reason for the pronounced anisotropy of the T dependence of the lattice parameters could be related to the fact that for $0 \leqslant x < 4$ the orthorhombic crystal structure is metastable, meaning that a structurally different polymorph exists, which is energetically more stable. This was explicitly shown for $1 \leqslant x \leqslant 2$, where a tetragonal crystal structure ($I4/mmm$) forms, when the crystals are grown from aqueous solution at lower temperatures [9]. Also for $x = 0$, we have found a tetragonal variant of Cs_2CuCl_4, if the crystal growth is carried out at $8\,°C$ [9,15]. For $x = 4$, the smaller anisotropy of $l_i(T)/l_i(280\,\text{K})$ indicates a more stable crystal structure, and indeed no different polymorph is known to exist so far for Cs_2CuBr_4.

The coefficients of the linear thermal expansion, α_i, are determined by taking the derivative of the normalized lattice parameters with respect to T, i.e.,

$$\alpha_i = \frac{1}{l_i(280\,\text{K})}\left(\frac{\partial l_i(T)}{\partial T}\right)_p.$$

We approximated these coefficients by using the fitted third-order polynomial function for $l_i(T)/l_i(280\,\text{K})$ in Fig. 3. As a consequence the accuracy at the high- and low-temperature ends (20 and 280 K) is limited. The T dependence of these calculated coefficients are shown in Fig. 4 for the four different concentrations. Representative error bars are shown in Fig. 4(b), which are estimated from the deviation of the polynomial function from the data points in Fig. 3. In Fig. 4, the above discussed anisotropy is even more visible. For $x = 0$, a pronounced maximum at around 170 K is apparent for the b axis [Fig. 4(a)], whereas the coefficient for the a axis is nearly constant. Going to $x = 1$ [Fig. 4(b)], the largest change appears for the a direction, where a broad maximum is observed above 150 K. We attribute this strongly anisotropic change to a preferred occupation of the Br atoms on the X2 site, which is the crystallographic site pointing along the a direction of the tetrahedron (cf. Fig. 5), because statistically distributed Br over the three different lattice sites would probably lead to similar changes for the three thermal expansion coefficients. Figure 4(c) presents the data for $x = 2$, here the most obvious change compared to the $x = 1$ sample appears along the c direction. Also this behavior is in agreement with the site-selective occupation, because for $1 \leqslant x \leqslant 2$, the X1 site is occupied by the Br atoms, which is the crystallographic site along the c direction of the tetrahedron (cf. Fig. 5). Finally, in Fig. 4(d), the coefficients of the thermal expansion are shown for Cs_2CuBr_4 with an overall reduced anisotropy.

For Cs_2CuCl_4, we can compare our data with thermal expansion coefficients, reported in the literature (Fig. 3 in Ref. [16]). These dilatometry data (not shown) were measured using a push-rod method [16] and the agreement with our data is satisfactorily good. Particularly, a broad maximum for the
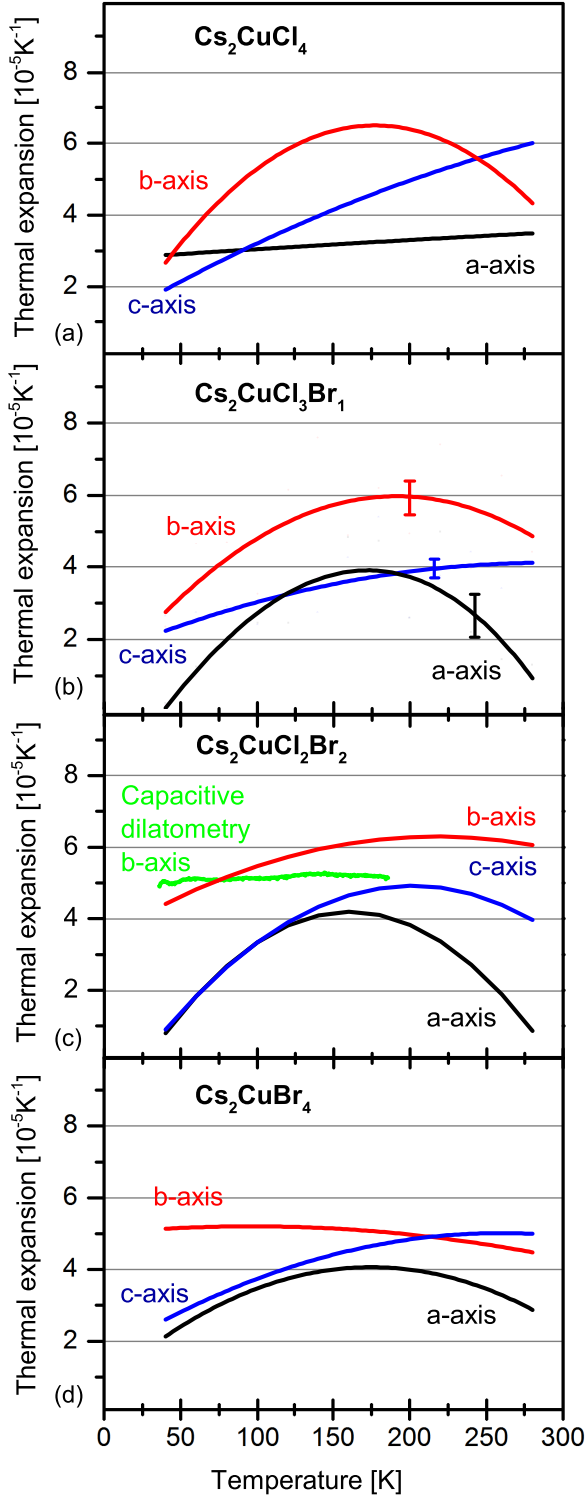
FIG. 4. (Color online) T dependence of the linear thermal expansion coefficients for (a) Cs_2CuCl_4, (b) $Cs_2CuCl_3Br_1$, (c) $Cs_2CuCl_2Br_2$, and (d) Cs_2CuBr_4. Typical errors correspond to the error bars shown in (b). The thermal expansion coefficients show a pronounced anisotropy for the three different crystal directions a, b, c and vary considerably with x. For $x = 2$, we compare the data determined from the lattice parameters with dilatometry data.

b direction (α_{33} in the notation of Ref. [16]) was observed around 180 K in accordance with our results in Fig. 4(a). In
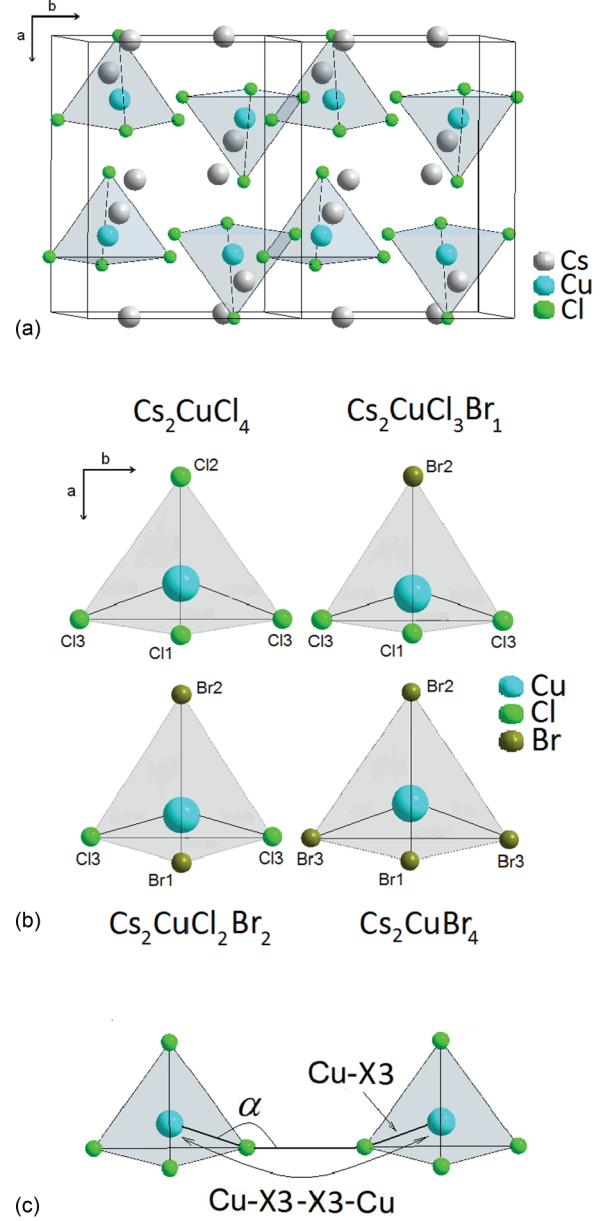

FIG. 5. (Color online) (a) Crystal structure for $x = 0$ with the $[CuX_4]$ tetrahedra for two neighboring unit cells along the b direction. (b) $[CuX_4]$ tetrahedron for the four investigated compositions calculated from the PXRD data at 20 K. All tetrahedra are shown in the ab plane and are normalized to their height. (b) Designation of the magnetic exchange path between two consecutive $[CuX_4]$ tetrahedra along the b direction with the angle α as well as the Cu-X3 and Cu-X3-X3-Cu distances used in Table III.

addition, we determined the thermal expansion coefficient for $Cs_2CuCl_2Br_2$ along the b axis using capacitive dilatometry. Within the errors, these data are in agreement with the results from PXRD as shown in Fig. 4(c).

IV. ANALYSIS OF THE $[CuX_4]$ TETRAHEDRA

The structurally most important unit for the magnetic exchange interactions in these materials is the $[CuX_4]$ tetrahedron ($X = $ Cl, Br), which determines the local environment

TABLE I. Lattice parameters and atomic positions for $x = 0, 1, 2, 4$ at 20 K, refined from PXRD data.

	Cs_2CuCl_4			$Cs_2CuCl_3Br_1$			$Cs_2CuCl_2Br_2$			Cs_2CuBr_4		
a (Å)	9.675(3)			9.819(7)			9.948(5)			10.069(7)		
b (Å)	7.496(2)			7.552(5)			7.633(3)			7.839(5)		
c (Å)	12.264(3)			12.408(1)			12.560(2)			12.758(1)		
Atom	x	y	z	x	y	z	x	y	z	x	y	z
Cs $4c$	0.132(3)	0.25	0.102(3)	0.131(1)	0.25	0.101(1)	0.128(1)	0.25	0.097(1)	0.124(1)	0.25	0.106(1)
Cs $4c$	0.502(3)	0.25	0.824(3)	0.510(1)	0.25	0.816(1)	0.510(1)	0.25	0.826(1)	0.496(1)	0.25	0.831(1)
Cu $4c$	0.221(8)	0.25	0.410(7)	0.234(4)	0.25	0.410(3)	0.243(3)	0.25	0.421(3)	0.224(4)	0.25	0.411(3)
Cl1 $4c$	0.332(1)	0.25	0.575(1)	0.317(4)	0.25	0.589(4)	–	–	–	–	–	–
Cl2 $4c$	−0.008(1)	0.25	0.381(1)	–	–	–	–	–	–	–	–	–
Cl3 $8d$	0.298(1)	−0.032(1)	0.357(1)	0.288(6)	0.006(6)	0.357(3)	0.291(3)	−0.001(4)	0.352(3)	–	–	–
Br1 $4c$	–	–	–	–	–	–	0.345(2)	0.25	0.580(2)	0.343(2)	0.25	0.585(2)
Br2 $4c$	–	–	–	−0.008(2)	0.25	0.384(2)	−0.011(2)	0.25	0.374(1)	−0.006(2)	0.25	0.377(2)
Br3 $8d$	–	–	–	–	–	–	–	–	–	0.298(1)	−0.013(3)	0.357(1)
χ^2_{red}	3.20			3.12			2.95			2.91		
wRp	0.095			0.098			0.087			0.085		
Rp	0.072			0.069			0.062			0.065		

of Cu [see Fig. 5(a)]. In this section, we will analyze the form of the tetrahedron in more detail for the different compositions of $Cs_2Cu(Cl_{4-x}Br_x)$ with $x = 0, 1, 2, 4$, refined from the low-temperature PXRD data. One important finding of our structural analysis is the site-selective occupation of the Br atoms on the three different halogen sites, illustrated in Fig. 5(b). This is already apparent from the development of the lattice parameters with x, shown in the first lines of Table I. Going from $x = 0$ to 1, the largest relative change occurs along the a direction, whereas the relative change of b is much smaller. Going from $x = 1$ to 2, the smallest increase is again for the b-direction, but much larger for a and c. The opposite is observed from $x = 2$ to 4, here the largest increase is found for the b direction, but much smaller relative changes of the a and c directions. Looking at the corners of the tetrahedron and its location within the crystal structure, it is clear that the X1 site will have the strongest influence for the c parameter (front corner), the X2 site for a (top corner), and the X3 sites for b (side corners) of the orthorhombic crystal structure as depicted in Fig. 5(b). Similar behavior was observed in the room-temperature PXRD data in Ref. [9].

The atomic positions refined from the PXRD data at 20 K are summarized in Table I. In a first attempt, a random distribution of the Cl and Br atoms was supposed for $x = 1$ and 2. However, with this configuration, it was not possible to get a reasonable agreement between the measured and simulated data. Therefore, in a second step, an ordered model with Br atoms on the X2 site for the $Cs_2CuCl_3Br_1$ compound and with the Br atoms on the X1 and X2 site for $Cs_2CuCl_2Br_2$ was assumed, as indicated from the development of the lattice parameters discussed above. With such a configuration, good agreement could be achieved with much lower χ_{red} values. Furthermore, no peculiarities were observed in the isotropic displacement parameters for the different atomic positions. Therefore, in Table I, we have split the halogen positions for Cl and Br. However, within the resolution of our PXRD data, we cannot completely rule out some Cl-Br site disorder in these compounds. From several measurements on different powdered crystals, we estimate an upper boundary of this

site-disorder of about 10%. This means for $Cs_2CuCl_2Br_2$ that at most every 10th Br-atom might sit on a X3 site. We like to note that for crystals grown directly from the melt at around 450 °C (Bridgman method), we could not observe this site-selective occupation of the Br atoms, but only a random distribution of the halogen atoms on the three different crystallographic positions [15]. To confirm our extended temperature-dependent PXRD measurements, we carried out neutron diffraction on a single crystal with dimensions of $2 \times 2 \times 1$ mm^3 of $Cs_2CuCl_3Br_1$ (cf. Table II). Obviously, the positions of the atoms could be refined with higher resolution compared to the PXRD data as shown in Table II, where we compare the structural data at 300 K for both methods. More important is the fact that within the given errors both methods reveal similar crystallographic positions.

TABLE II. Atomic positions for $Cs_2CuCl_3Br_1$ at 300 K, refined from single-crystal neutron diffraction and PXRD data.

	Neutron data		
Atom	x	y	z
Cs $4c$	0.13132(16)	0.25	0.10183(13)
Cs $4c$	0.49383(15)	0.25	0.82403(11)
Cu $4c$	0.23164(9)	0.25	0.41767(7)
Cl1 $4c$	0.34222(9)	0.25	0.57575(8)
Br2 $4c$	0.00292(10)	0.25	0.38095(8)
Cl3 $8d$	0.29338(7)	0.01202(7)	0.35627(6)
GOF		1.29	
	PXRD data		
Atom	x	y	z
Cs $4c$	0.132(1)	0.25	0.098(1)
Cs $4c$	0.510(1)	0.25	0.826(1)
Cu $4c$	0.221(3)	0.25	0.425(3)
Cl1 $4c$	0.337(4)	0.25	0.562(4)
Br2 $4c$	−0.005(2)	0.25	0.377(1)
Cl3 $8d$	0.291(3)	0.003(5)	0.367(3)
GOF		3.54	

TABLE III. Geometrical characteristics of the $[CuX_4]$ tetrahedra (X = Cl, Br) at 20 K, the given parameters are depicted in Fig. 5(c).

	Cs_2CuCl_4	$Cs_2CuCl_3Br_1$	$Cs_2CuCl_2Br_2$	Cs_2CuBr_4
α(Cu-X3-X3) (deg.), 280 K	151.9	152.9	159.3	155.8
α(Cu-X3-X3) (deg.), 20 K	154.9	155.1	152.8	153.9
d(Cu-X3) (Å), 280 K	2.204(8)	2.121(4)	2.312(3)	2.307(4)
d(Cu-X3) (Å), 20 K	2.336(8)	2.032(4)	2.154(3)	2.300(4)
d(X3-X3) (Å), 280 K	3.721(1)	3.871(6)	3.423(3)	3.746(4)
d(X3-X3) (Å), 20 K	3.262(1)	3.865(6)	3.799(3)	3.721(4)
d(Cu-X3-X3-Cu) (Å), 280 K	8.129(11)	8.113(8)	8.047(5)	8.360(6)
d(Cu-X3-X3-Cu) (Å), 20 K	7.934(11)	7.929(8)	8.107(5)	8.321(6)

Furthermore, the selective occupation of Br on the X2 site, was also observed in the neutron data.

In Fig. 5(b), we present the $[CuX_4]$ tetrahedra for the four different Br concentrations determined from the PXRD data at 20 K. The tetrahedra for $x = 0$ and 4 are distorted due to the Jahn-Teller effect, which is well established in these materials. On top of the Jahn-Teller distortion, the site-selective occupation of the Br atoms leads to an additional deformation for $x = 1$ and 2 evident from Fig. 5(b). $Cs_2CuCl_3Br_1$ has the Br atom on the crystallographic X2 site, leading to a $[CuCl_3Br_1]$ tetrahedron elongated along a, but compressed in its b direction. $Cs_2CuCl_2Br_2$ with the Br atoms on the X1 and X2 sites presents a $[CuCl_2Br_2]$ tetrahedron stretched along a and compressed along b. This nonlinear change with x of the tetrahedra has direct consequences on the low-temperature magnetic properties of these materials, which are determined mainly by the two in-plane exchange interactions J and J'. A first estimate of the dominant J can be gained by considering the length of the superexchange path along the b direction, depicted in Fig. 5(c). This Cu-X3-X3-Cu distance is determined by the bonding angle α and the distances Cu-X3 as well as X3-X3. These parameters are summarized in Table III, where the nonlinear development with x becomes apparent, in combination with a strongly varying temperature dependence (including positive and negative T coefficients). In the last line of Table III, the length of the spin superexchange

path from Cu to Cu along the b direction at 20 K is shown. From these data, one would expect a nearly unchanged J value for $x = 0$ and 1, followed by an increase of J towards $x = 4$. This structural argument is in agreement with susceptibility data on the same type of single crystals [10]. There it was shown that the maximum at around 3 K, which is primarily determined through J, is nearly unchanged for $0 \leqslant x \leqslant 1.5$, followed by a linear increase for $x \geqslant 2$.

In order to study, the influence of these strong structural variations with x and T on the magnetic interactions in more detail, a more accurate calculation of the spin superexchange coupling constants using density functional methods would be insightful. In the next section, we present DFT calculations for Cs_2CuCl_4 with the low-T structural data as input parameters
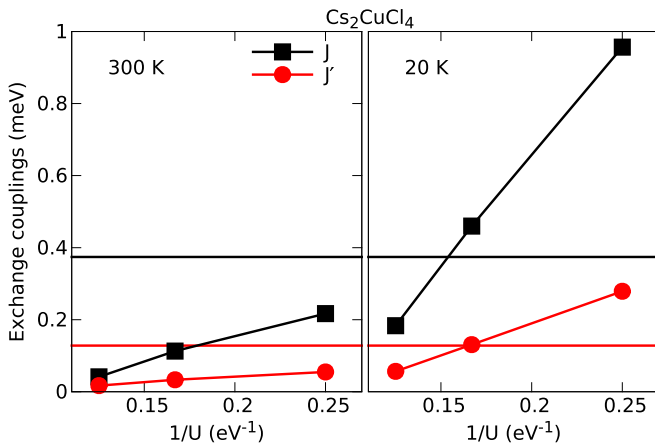

FIG. 6. (Color online) Spin exchange couplings for Cs_2CuCl_4 determined with density functional methods using two different sets of structural data, obtained at 300 and 20 K. Horizontal lines denote the experimental findings for J and J' [1].
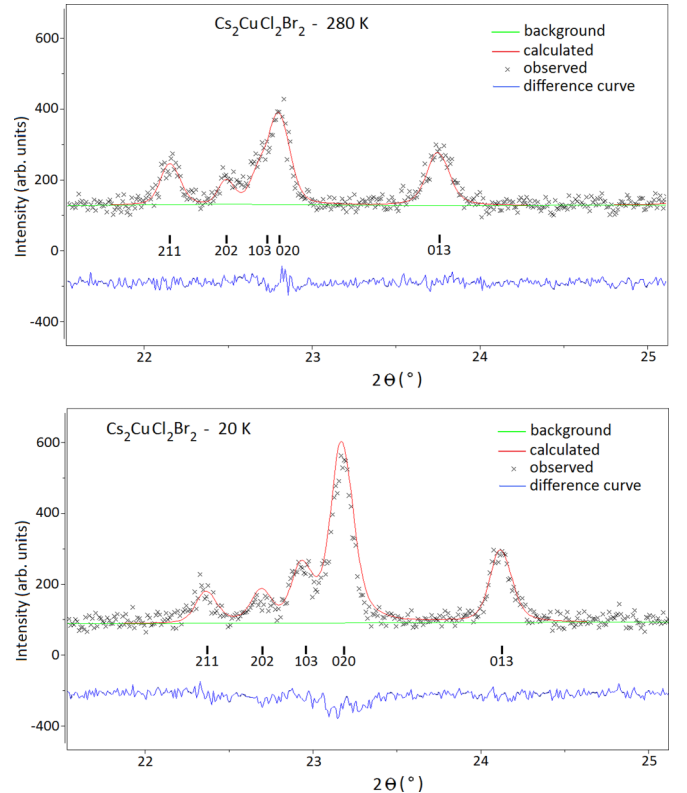

FIG. 7. (Color online) PXRD for $Cs_2CuCl_2Br_2$ at $T = 280$ (top) and 20 K (bottom). The difference curve between measured (crosses) and refined (red line) curve is shown as blue line. Ticks indicate the hkl peaks for the $Pnma$ structure.
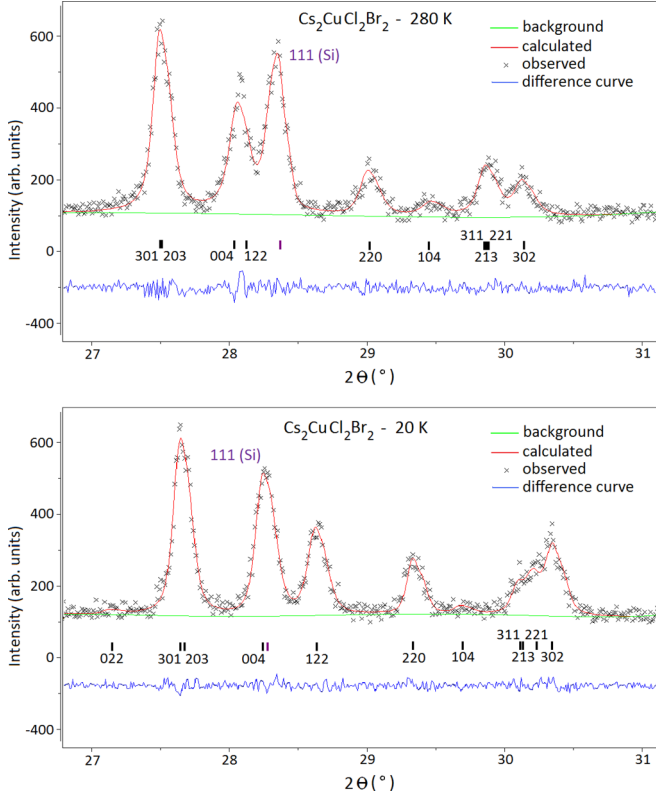
FIG. 8. (Color online) PXRD for $Cs_2CuCl_2Br_2$ at $T = 280$ (top) and 20 K (bottom). The difference curve between measured (crosses) and refined (red line) curve is shown as blue line. Ticks indicate the *hkl* peaks for the *Pnma* structure as well as for the 111 reflex of Si, used as internal standard.

and compare them with our earlier results, which were obtained from the room-temperature structure data.

V. DFT-BASED DERIVATION OF EXCHANGE-COUPLING CONSTANTS

To derive the spin superexchange coupling constants in Cs_2CuCl_4 within DFT, we employ the full-potential linearized augmented plane-waves method as implemented in the WIEN2K code [17]. The exchange and correlation effects are treated within the generalized gradient approximation [18] with an additional orbital-dependent term that mimics the on-site Coulomb repulsion between the Cu $3d$ electrons [19]. The coupling constants are calculated from the total energies of different Cu-spin configurations, assuming Ising-like interactions. In the present study, the spin superexchange couplings were obtained by performing total energy calculations with the generalized gradient approximation (GGA) and GGA $+ U$ functionals and by mapping the energy difference of various spin configurations onto a spin-$\frac{1}{2}$ Heisenberg model in the dimer approximation as described in Refs. [20] and [21]. For the calculations, we used the same $2 \times 2 \times 1$ supercell as in Ref. [11] and considered a ferromagnetic spin configuration together with seven antiferromagnetic (or ferrimagnetic) spin configurations given in Appendix C of Ref. [11]. We obtained seven superexchange couplings defined in Figs. 1(b) and 9(a) of Ref. [11]. Because the nearest-neighbor in-plane couplings
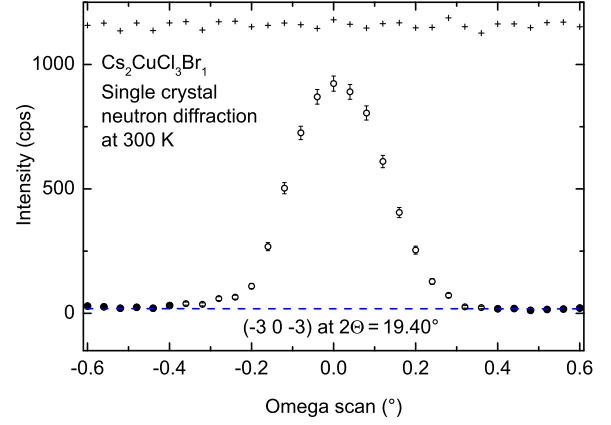

FIG. 9. (Color online) Measured omega scan around the $(\bar{3}0\bar{3})$ reflex using neutron diffraction on a $Cs_2CuCl_3Br_1$ single crystal. Circles represent the measured intensity with its statistical error. The closed circles are used to determine a linear interpolated background (dashed line). Crosses indicate the monitor of the neutron flux (divided by a factor 4), with an average value of 4638 cps.

J and J' are found for both temperatures to be considerably larger than the five other couplings, the latter will not be considered here explicitly.

In Fig. 6, we compare the spin superexchange couplings in Cs_2CuCl_4 calculated using the experimental crystal structures at 300 and 20 K from the presented PXRD data. No further structural relaxation was performed within DFT. For both temperatures, the leading magnetic interactions are by far the nearest-neighbor couplings J and J' within the triangular lattice. We calculated these two superexchange paths for three values of the on-site Coulomb repulsion $U = 4, 6$, and 8 eV. The realistic U value is close to 6 eV ($1/U = 0.17$ 1/eV). The temperature dependence of J and J', however, is remarkable, because these couplings from the 20 K structure are by a factor of ~ 3 larger than those from the 300 K structure, while their ratio $J'/J \sim 0.3$ remains roughly unchanged. Noticeably, the
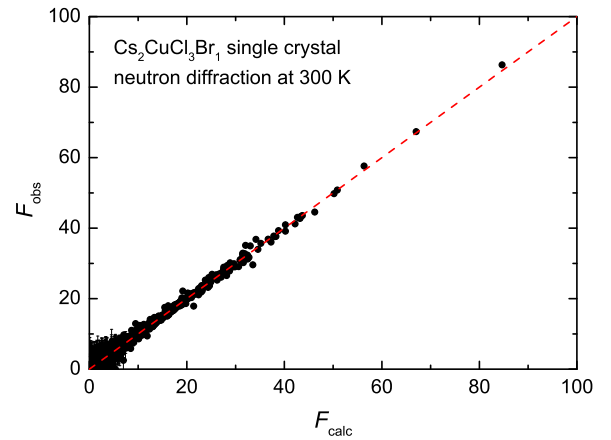

FIG. 10. (Color online) Outcome of the refinement from the neutron diffraction on a $Cs_2CuCl_3Br_1$ single crystal. Shown are the observed structure-factor amplitude F_{obs} versus the calculated structure-factor amplitude F_{calc} for the structural model given in Table II for all measured reflexes. A perfect agreement is indicated by the dashed line.

exchange couplings calculated from the 20 K structure are in good agreement with experimental estimates (based on neutron scattering data at 0.3 K from Ref. [1]), marked in Fig. 6 with horizontal lines of respective colors.

Comparing the structural data at 300 and 20 K, we can identify structural changes that can be responsible for such a pronounced variation of the leading exchange couplings. For instance, the interaction path J between two consecutive $[CuX_4]$ tetrahedra in the b direction is controlled by the Cu-X3-X3 angle α, the Cu-X3 distance and the Cu-X3-X3-Cu path length (see Table III). Remarkably, the variation with temperature of these particular structural parameters is significantly pronounced for Cs_2CuCl_4 and most probably the reason for the strong temperature dependence of J and J' evident from Fig. 6.

VI. CONCLUSIONS

We have presented a detailed low-temperature structural characterization of the triangular antiferromagnets $Cs_2Cu(Cl_{4-x}Br_x)$. Our measurements show a site-selective occupation of Br atoms on specific halogen sites, leading to a strong variation of the local Cu environment as a function of temperature and Br concentration. The temperature-dependent experimental structure data were then used as a starting point for calculating the magnetic coupling constants using density functional methods. This joint experimental and theoretical study reveals a strong temperature dependence of the magnetic interactions in Cs_2CuCl_4. Such behavior is caused by both, a large sensitivity of the exchange interactions to the structural details as well as the particularly nontrivial temperature dependence of the crystal structure. We believe that considering the so far ignored role of temperature-induced variations of spin superexchange couplings in Cs_2CuCl_4 may improve the understanding of its magnetic properties.

APPENDIX: REFINEMENT OF THE DIFFRACTION DATA

In this appendix, we present a selection of the raw diffraction data together with some more details about the refinement of these data. For the temperature dependent x-ray diffraction, we have selected two different data sets from Fig. 2(b) at 280 and 20 K. These data are shown in Figs. 7 and 8 for the 2Θ regions between 22–25 ° and 27–31 °, respectively. This detailed view allows to follow the pronounced changes with temperature and clearly shows that no structural transition is present when lowering temperature. To make this point even clearer, we have labeled each peak, which is important to distinguish between the Si peak (which shifts only slightly) and the peaks from the *Pnma* structure type. The former serves as the standard as described in the experimental section (Sec. II). The movement of the peaks from the *Pnma* structure type to higher angles when lowering the temperature is partially rather pronounced, reflecting directly the anisotropic thermal expansion, as discussed in detail in Sec. III. The overall difference curve in Figs. 7 and 8 is small, proving that our structural model describes the observed data very well which is reflected in the low χ_{red} values in Table I.

The neutron diffraction data, which we have carried out on a single crystal with $x = 1$, are shown in more detail in Figs. 9 and 10. A single measured ω profile of the $(\bar{3}0\bar{3})$ peak situated at $2\Theta = 19.40$ ° is presented in Fig. 9. From that profile the integrated intensity was obtained by summing over all the shown intensities and subtracting the background which was determined using a linear interpolated background of this peak with a Lehmann-Larsen algorithm [22]. For the refinement of the parameters presented in Table II we have used profiles from 1014 peaks. The quality of the overall refinement is visualized in Fig. 10, where the observed structure-factor amplitude, F_{obs}, is plotted against the calculated structure-factor amplitude, F_{calc}. The alignment of these points along the diagonal (dashed line) proves that the refined data is in excellent agreement with the structure model, resulting in the low GOF value in Table II.

[1] R. Coldea, D. A. Tennant, A. M. Tsvelik, and Z. Tylczynski, Phys. Rev. Lett. **86**, 1335 (2001).

[2] R. Coldea, D. A. Tennant, K. Habicht, P. Smeibidl, C. Wolters, and Z. Tylczynski, Phys. Rev. Lett. **88**, 137203 (2002).

[3] R. Coldea, D. A. Tennant, and Z. Tylczynski, Phys. Rev. B **68**, 134424 (2003).

[4] T. Radu, H. Wilhelm, V. Yushankhai, D. Kovrizhin, R. Coldea, Z. Tylczynski, T. Lühmann, and F. Steglich, Phys. Rev. Lett. **95**, 127202 (2005).

[5] T. Ono, H. Tanaka, H. Aruga Katori, F. Ishikawa, H. Mitamura, and T. Goto, Phys. Rev. B **67**, 104431 (2003).

[6] T. Ono *et al.*, J. Phys. Soc. Jpn. **74**, 135 (2005).

[7] S. Bailleul, D. Svoronos, P. Porcher, and A. Tomas, C. R. Acad. Sci. II **313**, 1149 (1991).

[8] B. Morosin and E. C. Lingafelter, Acta Crystallogr. **13**, 807 (1960).

[9] N. Krüger, S. Belz, F. Schossau, A. A. Haghighirad, P. Cong, B. Wolf, S. Gottlieb-Schoenmeyer, F. Ritter, and W. Assmus, Cryst. Growth Des. **10**, 4456 (2010).

[10] P. T. Cong *et al.*, Phys. Rev. B **83**, 064425 (2011).

[11] K. Foyevtsova, I. Opahle, Y.-Z. Zhang, H. O. Jeschke, and R. Valentí, Phys. Rev. B **83**, 125126 (2011).

[12] A. C. Larson and R. B. Von Dreele, Los Alamos National Laboratory Report No. LAUR 86-748 (1994).

[13] R. Pott and R. Schefzyk, J. Phys. E **16**, 444 (1983).

[14] V. Petricek, M. Dusek, and L. Palatinus, Z. Kristallogr. **229**, 345 (2014).

[15] N. van Well, Ph.D. thesis, Goethe-University Frankfurt, 2014.

[16] Z. Tylczynski, P. Piskunowicz, A. N. Nasyrov, A. D. Karaev, K. T. Shodiev, and G. Gulamov, Phys. Stat. Sol. (a) **33**, 133 (1992).

[17] K. Koepernik and H. Eschrig, Phys. Rev. B **59**, 1743 (1999).

[18] J. P. Perdew, K. Burke, and M. Ernzerhof, Phys. Rev. Lett. **77**, 3865 (1996).

[19] H. Eschrig, K. Koepernik, and I. Chaplygin, J. Solid State Chem. **176**, 482 (2003).

[20] T. Chanier, M. Sargolzaei, I. Opahle, R. Hayn, and K. Koepernik, Phys. Rev. B **73**, 134418 (2006).

[21] H. Jeschke *et al.*, Phys. Rev. Lett. **106**, 217201 (2011).

[22] M. S. Lehmann and F. K. Larsen, Acta Cryst. A **30**, 580 (1974).